Available online at www.sciencedirect.com
ScienceDirect
Journal of Power Sources 177 (2008) 339–347
JOURNAL OF POWER SOURCES
www.elsevier.com/locate/jpowsour

Polarization analysis for metal-supported SOFCs from different fabrication processes

Qiu-An Huang [a,b,1], Jörg Oberste-Berghaus [c], Dongfang Yang [d], Sing Yick [a], Zhenwei Wang [a], Bingwen Wang [b], Rob Hui [a,*]

[a] *Institute for Fuel Cell Innovation, National Research Council Canada, 4250 Wesbrook Mall, Vancouver, B.C. V6T 1W5, Canada*
[b] *Department of Control Science and Engineering, Huazhong University of Science and Technology, Wuhan, Hubei 430074, PR China*
[c] *Industrial Materials Institute, National Research Council Canada, 75 de Mortagne, Boucherville, Québec J4B 6Y4, Canada*
[d] *Industrial Materials Institute, National Research Council Canada, 800 Collip Circle, London, O.N. N6G 4X8, Canada*

Received 23 October 2007; received in revised form 29 November 2007; accepted 29 November 2007
Available online 5 December 2007

Abstract

Polarization characteristics of metal-supported solid oxide fuel cells, fabricated by pulsed laser deposition and suspension plasma spray, were investigated. With the electrochemical impedance spectroscopy and current–voltage polarization curves, the metal-supported SOFCs were compared and analyzed in terms of their cathode exchange current density, polarization loss and maximum power density over the temperature range of 400–600 °C. The electrochemical mechanism for the linear polarization characteristics observed from the experimental data was addressed. Results from experiments and simulation indicate that fabrication processes and operation temperatures play an important role in the electrochemical mechanism for linear polarization characteristics of metal-supported SOFCs.

Keywords: Metal-supported SOFCs; Electrochemical impedance spectroscopy; Polarization characteristics; Cathode exchange current density; Pulsed laser deposition; Suspension plasma spray

1. Introduction

Solid oxide fuel cells (SOFCs) are expected to be highly favoured for stationary power generation due to their high efficiency, low/zero pollution and fuel flexibility. However, high cost and low durability/reliability are major barriers in the path towards SOFC commercialization. It has been recognized that both these barriers are primarily due to the high temperatures of operation [1].

In an effort to overcome these barriers, recently, SOFCs with reduced operation temperature (500–850 °C) have received increasing interest. SOFCs operating at lower temperatures exhibit numerous advantages such as a wider choice of low-cost component materials, improved stability, and increased flexibility in the structure design [2]. As a representative of SOFC family, metal-supported SOFCs are expected to be more competitive than traditional energy conversion technologies due to the low cost, high strength, better workability, good thermal conductivity, and quicker start-up [3]. However, their performance is still relatively low at this current technology stage.

With respect to the development of reduced temperature SOFC technology, reducing electrolyte thickness and developing alternative materials with high-ion conductivity at reduced temperature are two major approaches. So far, various processing techniques, including spray pyrolysis (SP) [4,5], pulsed laser deposition (PLD) [6–8], and suspension plasma spray (SPS) [9,10], as well as spray and spin coating [11–13], have been extensively explored. These processing techniques have a significant effect on the SOFC interfacial morphology that in turn affects or determines the SOFC performance.

For performance improvement and component optimization of SOFCs, fundamental understanding of the correlation between fabrication processes and fuel cell reaction kinetics

* Corresponding author at: Institute for Fuel Cell Innovation, National Research Council Canada, 4250 Wesbrook Mall, Vancouver, B.C. V6T 1W5, Canada. Tel.: +1 604 221 3111; fax: +1 604 221 3001.
E-mail address: Rob.Hui@nrc-cnrc.gc.ca (R. Hui).
[1] Permanent address: Faculty of Physics and Electronic Technology, Hubei University, Wuhan, Hubei 430062, PR China.

0378-7753/$ – see front matter.
doi:10.1016/j.jpowsour.2007.11.092

including analysis of polarization characteristics seems to be necessary [14–19]. However, for metal-supported SOFCs, there is very little literature focusing on the fundamental understanding, in particular, through polarization analysis assisted by electrochemical impedance spectroscopy (EIS) [20].

In our previous work [8], EIS and electrochemical polarization were employed to investigate the performance and aging characteristics for metal-supported SOFCs, named Cell #1, with samarium doped ceria (SDC)/scandia-stabilized zirconia (ScSZ) bilayer as electrolytes, fabricated by PLD. However, in-depth analysis of the polarization characteristics was not pursued in that work. In the continuing effort to optimize the fabrication process and to improve the cell performance, a comprehensive analysis based on EIS data and polarization curves is given in this paper over the temperature range of 400–600 °C. Two representative metal-supported SOFC single cells, previous Cell #1 [8] and recently Cell #2 fabricated by suspension plasma spray, were chosen as examples for such a purpose.

2. Experimental procedures

Metal-supported SOFC single cells were fabricated using different deposition techniques. Commercially available porous SS430 and porous Hastelloy X alloys were adopted as substrates for selected Cell #1 and Cell #2, respectively. Porosity measurements of the SS430 and Hastelloy X were performed using the Archimedes method and their values were 22 and 28%, respectively. Cell #1 consists of NiO–SDC (50:50 wt.%) as the anode, ScSz and SDC bi-layer as the electrolyte, and $Sm_{0.5}Sr_{0.5}CoO_{3-\delta}$ (SSCo)–SDC (75:25 wt.%) as the cathode. Cell #2 consists of NiO–SDC (70:30 wt.%) as the anode, SDC as the electrolyte, and $Sm_{0.5}Sr_{0.5}CoO_{3-\delta}$ (SSCo)–SDC (75:25 wt.%) as the cathode. The active area is 0.23 cm^2 for Cell #1 and 0.34 cm^2 for Cell #2, respectively. The details about material, structure, and processing methods for both Cell #1 and Cell #2 are listed in Table 1.

Both cells were mounted on an alumina tube using Ceramabond 552 (Aremco). Pt meshes were used as both anode and cathode current collectors. Both cells were heated to 650 °C at 2 °C min^{-1} and dwelled at 650 °C for 5 h for the purpose of fully reducing the anodes by gradually raising the hydrogen concentration (maintaining 3% water stream). Subsequently, these two cells were heated to 800 °C at 3 °C min^{-1} to sinter the cathode for 30 min, and then cooled down to 400 °C at 2 °C min^{-1}. EIS and current–voltage–power curve were measured from 600 to 400 °C at interval of 50 °C.

Table 1
Summary of materials, structures, and processing methods for Cell #1 and Cell #2

Components	Substrate	Anode	Electrolyte	Cathode
Cell #1				
Material	SS430	NiO–SDC	ScSz/SDC	SSCo–SDC
Processing		Screen printing	PLD[a]	Screen printing
Thickness		90 μm	2/20 μm	25 μm
Cell #2				
Material	Hastelloy X	NiO–SDC	SDC	SSCo–SDC
Processing		SPS[b]	SPS	Screen printing
Thickness		30 μm	30 μm	45 μm

[a] Pulsed laser deposition.
[b] Suspension plasma spray.

Voltage–current (*I–V*) curves were measured using Solartron 1480A potentiostat with a scan rate of 4 mV s^{-1} in the potential range from open circuit voltage (OCV) to 0.3 V. EIS was measured over the frequency range of 100 kHz to 0.1 Hz with a Solartron 1260 frequency response analyzer (FRA) connected to a Solartron 1480A potentiostat. The perturbation amplitude was set to 50 mV at open circuit. The requirement of perturbation amplitude is determined by the internal characteristics of the investigated system, to a great extend, by the linearity degree of the investigated system. In theory, with smaller amplitude the system is perturbed, in better precision the linearization process could be implemented. In engineering, larger amplitude signal is expected because perturbation signal with smaller amplitude corresponds to stricter test requirement of high-signal noise ratio. SOFCs usually exhibit strong linearity over a large current polarization range. Consequently, signals with larger amplitude than the traditional 10 mV could be applied to impedance measurement for SOFCs with tolerable error. For each designed temperature of 600, 550, 500, 450 and 400 °C, both impedance and *I–V* data were measured twice at 10-min interval. All above measurements were under conditions of moist hydrogen as the fuel and dry air as the oxidant.

The tested cells were immersed into epoxy followed by solidification, and then sectioned and polished with different diamond slurries. The cross-sectional microstructures of two cells were then examined with a scanning electron microscope (SEM, Hitachi S-3500N) at two different resolutions described below.

3. Experimental results and discussions

3.1. Cell microstructures

In order to investigate microstructures affected by PLD and SPS, the two cells were characterized using SEM at different resolutions.

Fig. 1 clearly shows multi-layer microstructures of the cross-sections for Cell #1 and Cell #2 fabricated in lab scale. For both cells, the electrode layers are all porous, which are necessary for reactant gas feeds and diffuses. However, the interfaces between layers from the two cells are drastically different due to the processing methods.

In Fig. 1a and b for Cell #1, the AFL is much finer, not only extending the length of triple phase boundary to speed up the absorption/adsorption reaction of oxygen ion, but also enhancing the bonding of electrolyte/anode interface to reduce the interfacial contact resistance. Our previous work indicated that various microstructures, density and interfacial properties of bi-layer ScSZ/SDC film could be achieved by controlling the process parameters of PLD technique [7]. The bi-layer electrolyte ScSZ/SDC fabricated by PLD at a very low temperature is fine and dense without any pinholes or cracks, which not only improves OCV [9], but also meets the requirement of gas

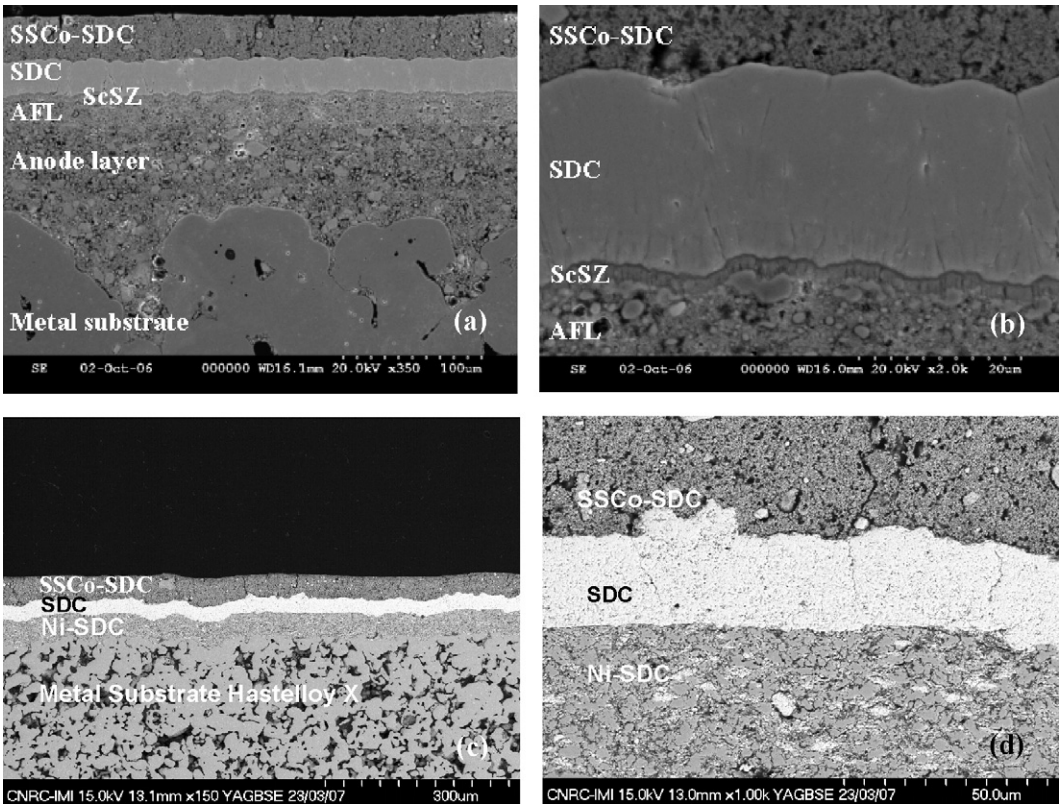

Fig. 1. Cross-sectional SEM images of the two tested cells: (a) 350× magnification for Cell #1; (b) 2000× magnification for Cell #1; (c) 150× magnification for Cell #2; (d) 1000× magnification for Cell #2.

tightness. From the SEM images in Fig. 1, it can be seen that no visible separation gaps between interfaces of both anode side and cathode side for Cell #1 can be found, suggesting the interface contacts are excellent.

Fig. 1c and d shows the microstructure of the cross-section for Cell #2 fabricated by SPS method, which has been well proven to be cost-effective and suitable for scale-up and offers an alternative technique to deposit SOFC functional layers on metal substrate [9]. Several tiny cracks are found in electrolyte layers for Cell #2, but none of them penetrated completely through the overall layer. In Fig. 1d, no clear interfacial gap can be found on both sides of the anode and the cathode for Cell #2, suggesting relative strong interfacial contact. However, compared with Cell #1, the interfacial bonding of Cell #2 seems not as compact as that of Cell #1. These interfacial differences could result in large differences in ohmic and polarization resistances of these two cells. This will be further discussed in Section 3.3.

3.2. Electrochemical polarization

Fig. 2 shows the voltage–current and power–current curves for both Cell #1 and Cell #2 over the temperature range of

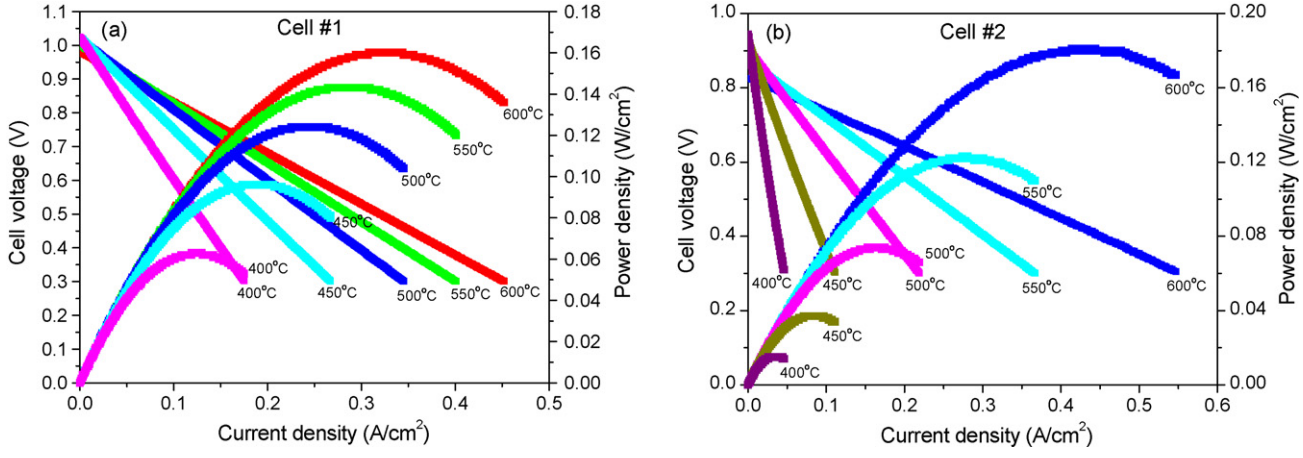

Fig. 2. Electrochemical polarization over the temperature range of 400–600 °C for Cell #1 (a) and Cell #2 (b).

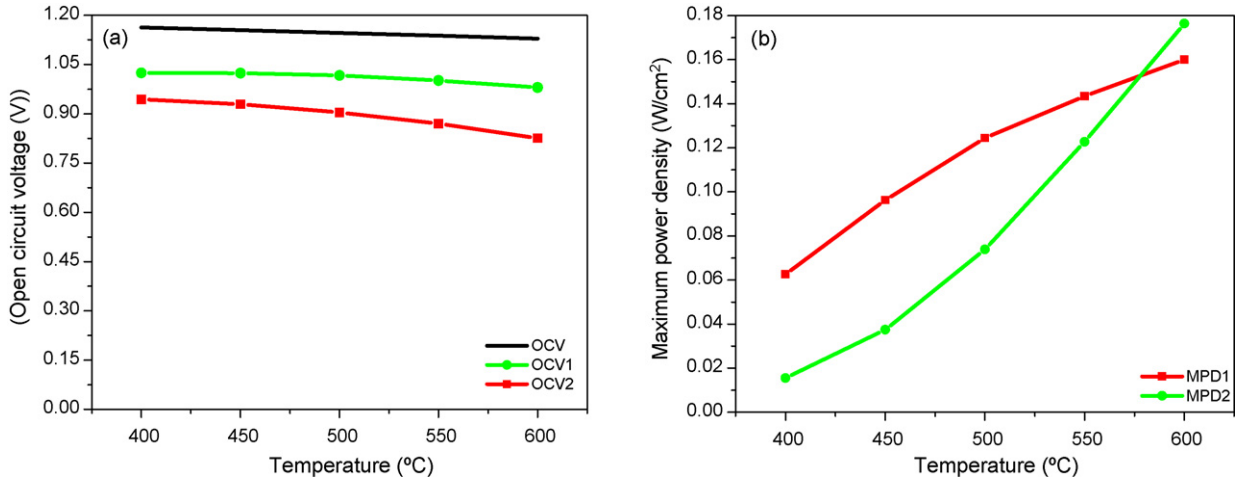

Fig. 3. (a) Theoretical and measured values for open circuit voltage, where OCV is for the theoretical value, OCV1 and OCV2 for the measured values of Cell #1 and Cell #2, respectively and (b) maximum power density of the metal-supported SOFCs over the temperature range of 400–600 °C.

400–600 °C. A thin ScSZ layer was employed for Cell #1 to block the electronic leaking from SDC electrolyte [8]. Cell #1 achieved an open circuit voltage (OCV) of 0.980–1.024 V, which is much higher than the OCV of 0.826–0.944 V for Cell #2 where only one single SDC layer of electrolyte was used. With respect to cell performance at the operation temperatures of 400, 450, 500, 550 and 600 °C, the maximum power densities of Cell #1 are 0.063, 0.096, 0.124, 0.144, and 0.160 W cm^{-2}, respectively. The maximum power densities of Cell #2 are 0.016, 0.037, 0.074, 0.123, and 0.181 W cm^{-2}, respectively.

Fig. 3a and b shows the theoretical open circuit voltage (OCV for theoretical value), the measured OCV (OCV1 for Cell #1 and OCV2 for Cell #2), and the measured maximum power density (MPD) related to operation temperatures for the two cells, respectively. As expected, the measured OCV of the two cells decrease slightly while the MPD of both cells increase dramatically with the increase of operation temperature. The difference between the theoretical values and the experimental ones for the OCV could be contributed from different sources, such as the porosity of the electrolyte layer, the electronic conductivity from SDC electrolyte, or the fuel leaking from the edge sealing. One point should be noted that MPD of Cell #2 exceeds that of Cell #1 at 600 °C although the measured OCV of Cell #2 is still lower than the measured OCV of Cell #1. In order to understand these phenomena, the electrochemical impedances for both Cell #1 and Cell #2 were measured under open circuit condition.

3.3. Electrochemical impedance measurement

EIS has been recognized as a powerful diagnostic tool to investigate fundamental processes and various polarization losses for SOFCs [20]. In order to understand and compare various polarization losses and associated reaction kinetics for both Cell #1 and Cell #2, electrochemical impedances were measured under open circuit condition over the temperature range of 400–600 °C. Nyquist plots for Cell #1 and Cell #2 over the temperature range of 400–600 °C are shown in Fig. 4a and b, respectively.

Ohmic resistances R_e and polarization resistances R_p of the two cells over the temperature range of 400–600 °C were

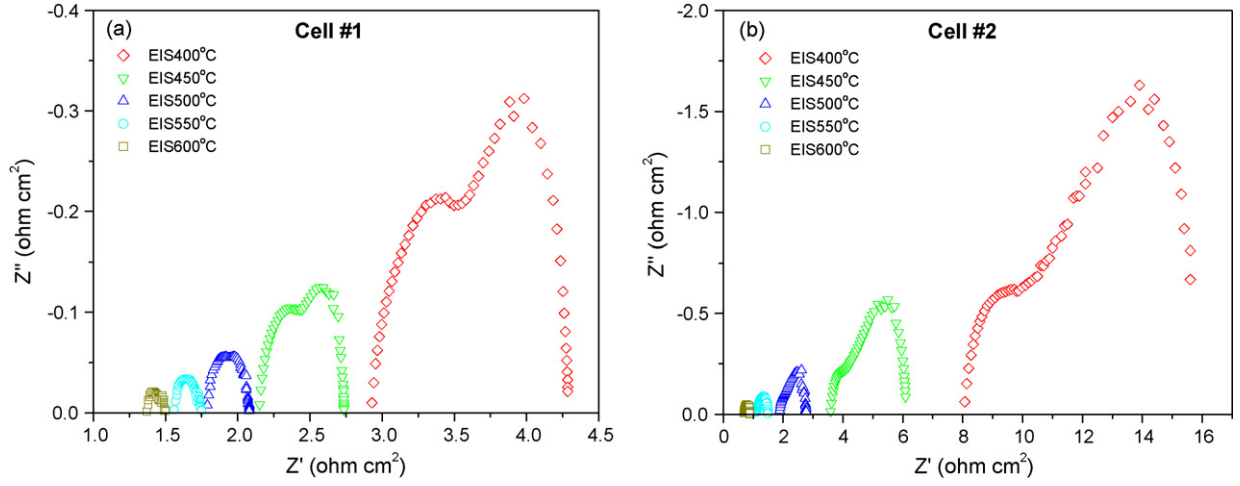

Fig. 4. The ac impedance spectra of two metal-supported cells under open circuit condition over the temperature range of 400–600 °C for Cell #1 (a) and Cell #2 (b).

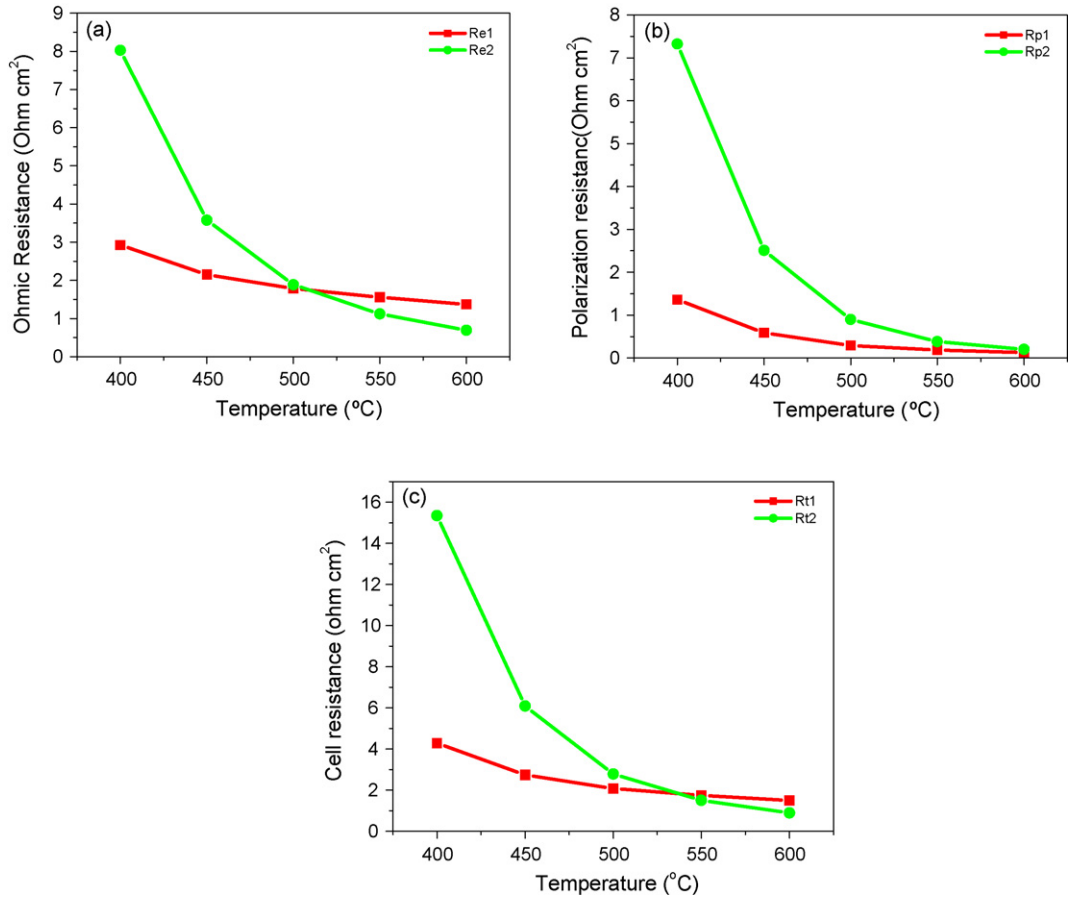

Fig. 5. (a) Ohmic resistances, (b) polarization resistances and (c) cell resistances of the two metal-supported cells over the temperature range of 400–600 °C under open circuit condition.

extracted from the measured Nyquist plots in Fig. 4, assuming cell resistance $R_t = R_p + R_e$. Generally speaking, the main contributor to R_e is from the electrolyte [21]. Fig. 5a–c shows curves of R_e, R_p, and R_t as a function of the operation temperature for the two cells, respectively. It can be seen that both of R_e and R_p of the two cells decrease with the increase of measurement temperature. Both R_e and R_p of Cell #2 are obviously greater than those of Cell #1 over the low temperature range of 400–500 °C likely due to Cell #2 with weaker bonding of the electrolyte–electrode interfaces than that of Cell #1 as shown in Fig. 1. However, R_e, R_p, and R_t of Cell #2 are more sensitive to the change of temperature than those of Cell #1 due to the energy difference of processing between PLD and SPS. The impact from fabrication processes becomes less important when the reaction kinetics get enhanced at elevated temperature. Consequently, over 550 °C, the large difference in polarization resistance for the two cells gradually disappears and almost converges to a small value. In this situation, ohmic loss dominates the overpotential losses. At 600 °C, the ohmic resistance of Cell #2 becomes lower than that of Cell #1 and this is most likely due to the low-ionic conductivity of ScSZ in the bi-layer electrolytes and the potential reaction between ScSz and SDC in Cell #1 [7]. The lower cell resistance of Cell #2 is in agreement with the phenomenon in Section 3.2, where MPD of Cell #2 exceeds that of Cell #1 at 600 °C although the OCV of Cell #2 is still lower than that of Cell #1.

3.4. Modeling of cell polarization

3.4.1. Analysis of polarization characteristics

In the simplest case, the electrochemical processes characterized for Cell #1 and Cell #2 in Fig. 4 can be simulated by an equivalent circuit model (ECM) in Fig. 6a [22], where (R_1C_1) simulating high-frequency processes, (R_2C_2) medium frequency processes, R_{ohm} ohmic resistance mainly consisting of electrolyte resistance and various contact resistances, L an

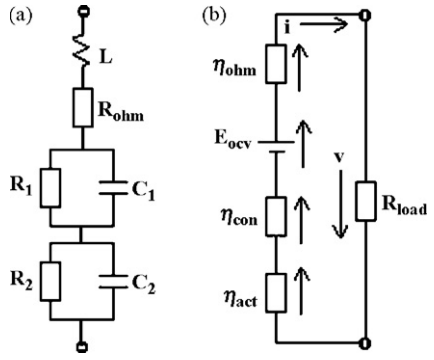

Fig. 6. Two equivalent circuit models (ECM) for metal-supported SOFC: (a) ECM to simulate the electrochemical processes under open circuit condition and (b) ECM to analyze *I–V* polarization characteristics.

inductance introduced by connecting conductor. The time constants of the electrochemical processes are given by RC and can be determined through frequency response measurements [23]. It is also well known that I–V characteristics reflect the overlapped effect of ohmic polarization, concentration polarization, and activation polarization. Hence, dc measurement and analysis of steady-state I–V characteristics are effective ways to investigate kinetics for SOFCs [21], although the capacitive and inductance parts in Fig. 6a could not be reflected in I–V characteristics. The ECM in Fig. 6b is applied to analyze I–V polarization characteristics for Cell #1 and Cell #2 [24], where E_{ocv} open circuit voltage, η_{act} activation polarization, η_{con} concentration polarization, η_{ohm} ohmic polarization, R_{load} load resistance, V cell voltage, i current density.

Previous experimental results [25,26] suggested the overpotential on the anode side was extremely small in comparison to the one on the cathode side. Thus, activation polarization and concentration polarization from the anode side could be ignored for simplification of the analysis. As a result, cell voltage $V(i) = E_{ocv} - \eta_{act} - \eta_{ohm} - \eta_{con,c}$ can be simplified.

$$V(i) = E_{ocv} - \eta_{act,c} - \eta_{ohm} - \eta_{con,c} \tag{1}$$

In this work, flow rates of fuel and oxidant were held high enough compared to the stoichiometry required by the corresponding current density, thus concentration polarization could be simply treated either as a constant or be ignored. This allows further cell voltage simplification:

$$V(i) = E_{ocv} - \eta_{act,c} - \eta'_{ohm} \tag{2}$$

where $\eta'_{ohm} = \eta_{ohm} + \eta_{con,c}$. The activation polarization for the cathode is normally expressed by the well-known Butler–Volmer equation [23]

$$i = i_{0,c}\left\{\exp\left(\frac{\beta n_e F\eta_{act,c}}{RT}\right) - \exp\left(-\frac{(1-\beta)n_e F\eta_{act,c}}{RT}\right)\right\} \tag{3}$$

where i is current density (mA cm^{-2}), $i_{0,c}$ cathode exchange current density (mA cm^{-2}), β the transfer coefficient (usually 0.5) [27], n_e electrons transferred per reaction (here 2), F Faraday constant (96,485 C mol^{-1}), $\eta_{act,c}$ cathode activation polarization (V), R universal gas constant (8.314 J mol^{-1} k^{-1}), T temperature (K). If we defined $\eta_0(T)$ as

$$\eta_0(T) = \frac{RT}{\beta n_e F} \tag{4}$$

Then, Eq. (3) can be expressed as

$$i = i_{0,c}\left\{\exp\left(\frac{\eta_{act,c}}{\eta_0(T)}\right) - \exp\left(-\frac{\eta_{act,c}}{\eta_0(T)}\right)\right\} \tag{5}$$

For high-activation polarization, it is possible that

$$\eta_{act,c} \gg \eta_0(T) \tag{6}$$

In such case, Eq. (3) can be simplified as the logarithmic current–potential relation.

$$\eta_{act,c} = -\frac{RT}{\beta n_e F}\ln i_{0,c} + \frac{RT}{\beta n_e F}\ln i \tag{7}$$

Eq. (7) is the well-known Tafel equation for the cathode. One point has to be noted that Eq. (7) is only valid for $i > i_{0,c}$ [28].

For low-activation polarization, it is possible that

$$\eta_{act,c} \ll \eta_0(T) \tag{8}$$

In such case, Butler–Volmer equation can be simplified as the linear current–potential relation in terms of Taylor series expansion.

$$\eta_{act,c} = i\frac{RT}{n_e F i_{0,c}} \tag{9}$$

By differentiating Eq. (9), we can define

$$R_{ct,c}^{ocv} = \frac{^{def}\partial\eta_{act,c}}{\partial i} = \frac{RT}{n_e F i_{0,c}} \tag{10}$$

where $R_{ct,c}^{ocv}$ is cathode charge transfer resistance under open circuit condition [29,30]. When both concentration polarization of the whole cell and activation polarization on the anode side are neglected as discussed above, polarization resistances R_p obtained from EIS measurement under open circuit condition for Cell #1 and Cell #2 can be approximately regarded as $R_{ct,c}^{ocv}$, i.e.

$$R_{ct,c}^{ocv} \approx R_p \tag{11}$$

Based on Eq. (10) and the approximation of $R_{ct,c}^{ocv}$ via Eq. (11), the cathode exchange current density $i_{0,c}$ could be calculated. The calculated exchange current density $i_{0,c}$ and the current density i^* corresponding to MPD for Cell #1 and Cell #2 over the temperature range of 400–600 °C are listed in Table 2. It is obvious that cathode exchange current density $i_{0,c}$ increases dramatically with the increase in operating temperatures for both cells, so does the current density i^*, and the $i_{0,c}$ for Cell #1 is greater than the $i_{0,c}$ for Cell #2 at given temperatures. Subsequently, the increase of the cathode exchange current density $i_{0,c}$ as a function of temperature extend the range of current density that is not valid for the Tafel equation, but is still valid for linear activation polarization via Eq. (9) as discussed above. Moreover, the induced cathode exchange current density, as functions of both operation temperatures and fabrication processes, offers a viewpoint to reveal the polarization related to operating temperatures, fabrication processes, and materials properties for SOFCs.

Table 2
Calculated exchange current density for cathode and measured current density corresponding to MPD at operation temperatures from 400 to 600 °C

	Temperature (°C)				
	400	450	500	550	600
Cell #1					
$i_{0,c}$ (mA cm^{-2})[a]	21.3	53.0	114.1	190.2	298.1
i^* (mA cm^{-2})[b]	108.0	173.0	225.0	263.0	308.0
Cell #2					
$i_{0,c}$ (mA cm^{-2})	4.0	12.4	37.0	92.5	184.7
i^* (mA cm^{-2})	26.0	71.0	153.0	257.0	414.0

[a] Cathode exchange current density (mA cm^{-2}).
[b] Current density corresponding to MPD (mA cm^{-2}).

Table 3
Calculated values of $\eta_0(T)$, η^*_{1act} and η^*_{2act} at operation temperatures of 400–600 °C

	Temperature (°C)				
	400	450	500	550	600
$\eta_0(T)$ (mV)[a]	58.0	62.3	66.6	70.9	75.2
$\eta^*_{1act,c}$ (mV)[b]	136.5	99.2	66.7	48.3	40.5
$\eta^*_{2act,c}$ (mV)[c]	173.3	160.1	133.6	108.1	102.1

[a] $\eta_0(T) = \frac{RT}{\beta n_e F}$.
[b] Cathode activation polarization at current density i^* for Cell #1.
[c] Cathode activation polarization at current density i^* for Cell #2.

With Eq. (2), we can get $\eta_{act,c}(i) = E_{ocv} - V(i) - \eta'_{ohm}(i)$, where i is current density at different temperatures of 400–600 °C as listed in Table 2, $\eta'_{ohm}(i) \approx i\,R_{ohm}$, R_{ohm} ohmic resistance obtained from EIS measurement. Consequently, we could approximately calculate $\eta_{act,c}(i)$ at different temperatures of 400–600 °C in order to investigate the cathode activation polarization over the current density range of $0 \sim i^*$. The values of $\eta_0(T)$, η^*_{1act} and η^*_{2act} at current density of i^* over the temperature range of 400–600 °C were listed in Table 3. The calculated results listed in Table 3 indicated that Eq. (8) was not strictly applicable at current density of i^*. Two special situations including high-activation polarization and low-activation polarization have been discussed previously [27,31]. In terms of the applicable range of these two simplified activation models via Eqs. (7) and (9) discussed by Chan et al. [27], the low-activation polarization situation is more suitable to the calculated cathode activation polarization $\eta^*_{act,c}$ at current density i^*. On one hand, activation polarization corresponding to the current density i^* is maximized in the range of $0 \sim i^*$. On the other hand, considering the activation polarizations on the anode side and concentration polarization of the cell are ignored, the calculated cathode activation polarization $\eta_{act,c}$ is expected to be greater than the actual activation polarization. As a result, with respect to the investigated current density range of $0 \sim i^*$, it is reasonable to employ linear model via Eq. (9) to approximate the activation polarization of Cell #1 and Cell #2. The reduction of the activation polarization with increase of temperature strengthens the linearity of activation polarization as indicated in Eq. (8). Table 3 suggests that Cell #1 exhibited less activation polarization than Cell #2 at each a given temperature.

3.4.2. Fitting of polarization curves

According to the discussion for the activation polarization above, Eq. (2) can be completely linearized over the investigated current range of $0 \sim i^*$ (mA).

$$V(i) = E_{ocv} - iR_{act,c} - iR_{ohm} = E_{ocv} - iR_t \tag{12}$$

where

$$R_t = R_{act,c} + R_{ohm} \tag{13}$$

With the measured current–voltage data and approximated Eq. (12), the fitted values of parameters such as open circuit voltage E'_{ocv} and cell resistance R'_t could be obtained through the fitting function Polyfit in Matlab, as listed in Tables 4 and 5, respectively. Subsequently, the normalized and accumulated-residuals (NA-Res) of I–V curve fitting with Eq. (12) over the temperature range of 400–600 °C are calculated via

$$\text{NA} - \text{Res} = \frac{100}{N}\sum_i |V_{measured} - V_{calculated}|_T \tag{14}$$

where $V_{measured}$ is the measured value of cell voltage, $V_{calculated}$ the calculated value of cell voltage via Eq. (12) with parameters from I–V curve fitting, N the number of data points for current density range of $0 \sim i^*$ and T is the temperature.

Tables 4 and 5 indicated that the fitted cell resistance and open circuit voltage agreed well with the measured cell resistance and open circuit voltage. Table 6 shows that normalized

Table 4
Fitted E'_{ocv} and measured E_{ocv} at operation temperatures of 400–600 °C

	Temperature (°C)				
	400	450	500	550	600
Cell #1					
E_{ocv}[a] (V)	1.0244	1.0238	1.0167	1.0014	0.9801
E'_{ocv}[b] (V)	1.0241	1.0247	1.0180	1.0023	0.9813
Cell #2					
E_{ocv} (V)	0.9440	0.9291	0.9040	0.8701	0.8258
E'_{ocv} (V)	0.9404	0.9257	0.9054	0.8740	0.8316

[a] Measured OCV.
[b] Fitted OCV from I–V curves.

Table 5
Fitted R'_t and measured R_t at operation temperatures of 400–600 °C

	Temperature (°C)				
	400	450	500	550	600
Cell #1					
R_t[a] ($\Omega\,cm^2$)	4.2854	2.7360	2.0784	1.7459	1.4951
R'_t[b] ($\Omega\,cm^2$)	4.2273	2.7348	2.0856	1.7498	1.5025
Cell #2					
R_t ($\Omega\,cm^2$)	15.3496	6.0884	2.7851	1.5042	0.8961
R'_t ($\Omega\,cm^2$)	14.8022	5.8597	2.7918	1.5564	0.9511

[a] Cell resistance from EIS measurement under open circuit condition.
[b] Cell resistance from I–V fitting via Eq. (12).

Table 6
Normalized and accumulated-residuals (NA-Res) of I–V fitting at operation temperatures of 400–600 °C

	Temperature (°C)				
	400	450	500	550	600
NA-Res[a] (V)					
Cell #1	0.1334	0.0735	0.0555	0.0462	0.0398
Cell #2	0.4052	0.2195	0.0932	0.0855	0.1406

[a] $\text{NA} - \text{Res} = \frac{100}{N}\sum_i |V_{measured} - V_{calculated}|_T$.

Table 7
Measured MPD and simulated MPD′ at different operational temperatures of 400–600 °C

	Temperature (°C)				
	400	450	500	550	600
Cell #1					
MPD[a] ($W\,cm^{-2}$)	0.0626	0.0963	0.1244	0.1435	0.1600
MPD′ [b] ($W\,cm^{-2}$)	0.0606	0.0937	0.1220	0.1432	0.1633
Cell #2					
MPD ($W\,cm^{-2}$)	0.0155	0.0374	0.0738	0.1227	0.1810
MPD′ ($W\,cm^{-2}$)	0.0159	0.0395	0.0811	0.1404	0.2186

[a] Measured MPD.
[b] Simulated MPD.

and accumulated-residuals of linear fitting are quite small with ranges from 0.0398 to 0.4052 V related to each 100 current points at the temperatures of 400–600 °C. The fitting residuals for both cells decrease with the increase of operating temperatures. This trend is consistent with the result in Table 2. The only exception occurs at the temperature of 600 °C for Cell #2, which is most likely due to the instability of newly fabricated metal-supported cell. Moreover, the normalized and accumulated-residuals NA-Res of Cell #1 is much lower than that of Cell #2 at each given temperature. All these results strongly suggest that the approximation and discussion on the activation polarization and *I–V* characteristics above is reasonable and feasible.

With the fitted open circuit voltage E'_{ocv} and cell resistance R'_t through fitting at temperatures of 400–600 °C, the cell MPD can be predicted in terms of $P_{max} = (1/2)({E'_{ocv}}^2/R'_t)$conveniently. As indicated in Table 7, Cell #1 exhibits higher precision in MPD prediction than Cell #2 at given operation temperatures. This result is also consistent with the conclusion drawn from Table 6 for Cell #1 and Cell #2 over the temperature range of 400–600 °C. The above analysis of polarization characteristics related to operating temperatures and fabrication processes is based on fitting residuals rather than the intermediate variables including fitted resistance and voltage, or by-production such as the predicted MPD.

4. Conclusions

Polarization characteristics related to fabrication processes and operating temperatures have been investigated for metal-supported SOFCs fabricated by PLD and SPS, respectively. With EIS and current–voltage polarization curves, the electrochemical mechanism for the linear polarization characteristics of the metal-supported SOFCs has been addressed in terms of cathode exchange current density, polarization loss and maximum power density over the temperature range of 400–600 °C. Experimental and simulating results indicated that high-operating temperatures could extend the range of current density with linear activation polarization, and low-activation polarization due to fabrication processes could also strengthen the linearity of activation polarization. In summary, fabrication processes and operating temperatures play an important role in the linearity of the polarization characteristics of metal-supported SOFCs. The presented method in this manuscript also offers a viewpoint to reveal the polarization characteristics of SOFCs related to materials properties, fabrication processes, and operation temperatures.

Acknowledgements

Thanks to the National Fuel Cell and Hydrogen Program of the National Research Council (NRC) Canada for the financial support for this work. The authors would also like to thank Dr. Jiujun Zhang and Mr. Justin Roller at NRC for the review and discussion of the manuscript. Mr. Qiu-An Huang, a Ph.D. candidate, appreciates China Scholarship Council and NRC for providing living allowances as well.

References

[1] J.P.P. Huijsmans, F.P.F. van Berkel, G.M. Christie, J. Power Sources 71 (1998) 107–110.
[2] F. Nishiwaki, T. Inagaki, J. Kano, J. Akikusa, N. Murakami, K. Hosoi, J. Power Sources 157 (2006) 809–815.
[3] M.C. Tucker, G.Y. Lau, C.P. Jacobson, L.C. DeJonghe, S.J. Visco, J. Power Sources 171 (2007) 477–482.
[4] P.S. Patil, Mater. Chem. Phys. 59 (1999) 185–198.
[5] D. Perednis, L.J. Gauckler, Solid State Ionics 166 (2004) 229–239.
[6] J. Will, A. Mitterdorfer, C. Kleinlogel, D. Perednis, L.J. Gauckler, Solid State Ionics 131 (2000) 79–96.
[7] D. Yang, X. Zhang, S. Nikumb, C. Decès-Petit, R. Hui, R. Maric, D. Ghosh, J. Power Sources 164 (2007) 182–188.
[8] R. Hui, D. Yang, Z. Wang, S. Yick, C. Decès-Petit, W. Qu, A. Tuck, R. Maric, D. Ghosh, J. Power Sources 167 (2007) 336–339.
[9] R. Hui, Z. Wang, O. Kesler, L. Rose, J. Jankovic, S. Yick, R. Maric, D. Ghosh, J. Power Sources 170 (2007) 308–323.
[10] Z. Wang, J.O. Berghaus, S. Yick, C. Decès-Petit, W. Qu, R. Hui, R. Maric, D. Ghosh, J. Power Sources 176 (2008) 90–95.
[11] T. Suzuki, I. Kosacki, H.U. Anderson, Solid State Ionics 151 (2002) 111–121.
[12] H.U. Anderson, M.M. Nasrallah, C.C. Chen, U.S. Patent, 5,494,700 (1996).
[13] R. Hui, Z.W. Wang, S. Yick, R. Maric, D. Ghosh, J. Power Sources 172 (2007) 840–844.
[14] G.M. Christie, F.P.F. van Berkel, Solid State Ionics 83 (1996) 17–27.
[15] W. Bai, K.L. Choy, R.A. Rudkin, B.C.H. Steele, Solid State Ionics 113–115 (1998) 259–263.
[16] T. Suzuki, I. Kosacki, H.U. Anderson, P. Colomban, J. Am. Ceram. Soc. 84 (2001) 2007–2014.
[17] J.L.M. Rupp, L.J. Gauckler, Solid State Ionics 177 (2006) 2513–2518.
[18] A. Tschöpe, R. Birringer, J. Electroceram. 7 (2001) 167–177.
[19] R. Hui, J. Roller, S. Yick, X.G. Zhang, C.D. Petit, Y.S. Xie, R. Maric, D. Ghosh, J. Power Sources 172 (2007) 493–502.
[20] Q.A. Huang, R. Hui, B. Wang, J. Zhang, Electrochim. Acta 52 (2007) 8144–8164.
[21] S.B. Adler, Chem. Rev. 104 (2004) 4791–4843.
[22] Z.W. Wang, M.J. Cheng, Y.L. Dong, M. Zhang, H.M. Zhang, J. Power Sources 156 (2006) 306–310.
[23] S.C. Singhal, K. Kendal, High Temperature Solid Oxide Fuel Cells Fundamentals Design and Applications, Elsevier Ltd., Oxford, England, 2003.
[24] T.A. Aloui, K. Halouani, Appl. Therm. Eng. 27 (2007) 731–737.
[25] C.R. Xia, M.L. Liu, Adv. Mater. 14 (2002) 521–523.
[26] T. Kato, K. Nozaki, A. Negishi, K. Kato, A. Momma, Y. Kaga, S. Nagata, K. Takano, T. Inagaki, H. Yoshida, et al., J. Power Sources 133 (2004) 169–174.
[27] S.H. Chan, K.A. Khor, Z.T. Xia, J. Power Sources 93 (2001) 130–140.

[28] J. Larminie, A. Dicks, Fuel Cell Systems Explained, second edition, John Wiley & Sons, Chichester, England, 2003.
[29] J.L. Zhang, Y.H. Tang, C.J. Song, J.J. Zhang, H.J. Wang, J. Power Sources 163 (2006) 532–537.
[30] C.J. Song, Y.H. Tang, J.L. Zhang, J.J. Zhang, H.J. Wang, J. Shen, S. McDermid, J. Li, P. Kozak, Electrochim. Acta 52 (2007) 2552–2561.
[31] D.A. Noren, M.A. Hoffman, J. Power Sources 152 (2005) 175–181.